Available online at www.sciencedirect.com
ScienceDirect
Acta Materialia 56 (2008) 2073–2088
Acta MATERIALIA
www.elsevier.com/locate/actamat

The temporal evolution of the decomposition of a concentrated multicomponent Fe–Cu-based steel

R. Prakash Kolli *, David N. Seidman

Department of Materials Science and Engineering, Northwestern University, Northwestern University Center for Atom-Probe Tomography (NUCAPT), Evanston, IL 60208, USA

Received 7 August 2007; received in revised form 28 December 2007; accepted 31 December 2007
Available online 4 March 2008

Abstract

The nucleation (to a limited extent), growth and coarsening behavior of Cu-rich precipitates in a concentrated multicomponent Fe–Cu-based steel aged at 500 °C from 0.25 to 1024 h is investigated. The temporal evolution of the precipitates, heterophase interfaces, matrix compositions and precipitate morphologies are presented. With increasing time, Cu partitions to the precipitates, Ni, Al and Mn partition to the interfacial region, whereas Fe and Si partition to the matrix. Coarsening time exponents are determined for the mean radius, $\langle R(t)\rangle$, number density, $N_V(t)$, and supersaturations, which are compared to the Lifshitz–Slyzov–Wagner (LSW) model for coarsening, modified for concentrated multicomponent alloys by Umantsev and Olson (UO). The experimental results indicate that the alloy does not strictly follow UO model behavior. Additionally, we delineate the formation of a Ni–Al–Mn shell with a stoichiometric ratio of 0.51:0.41:0.08 at 1024 h, which reduces the interfacial free energy between the precipitates and the matrix.
© 2008 Acta Materialia Inc. Published by Elsevier Ltd. All rights reserved.

Keywords: Coarsening; Fe–Cu alloy; Phase separation; Atom-probe tomography; Interfacial segregation

1. Introduction

Copper precipitation-strengthened structural steels are of considerable commercial importance due to their high strength, good impact toughness, excellent weldability without preheat or postheat, and corrosion resistance [1–4]. This desirable combination of properties is derived from Cu precipitates formed within these steels after solutionizing and thermal aging. The sequence of precipitation, structure and composition has been studied by Mössbauer spectroscopy [5], field-ion microscopy (FIM) [6,7], atom-probe field-ion microscopy (APFIM) [8–11], atom-probe tomography (APT) [12], conventional and high-resolution electron microscopies (CTEM and HREM) [11,13–20], small-angle neutron scattering (SANS) [21–24], extended X-ray absorption fine structure (EXAFS) [25], X-ray absorption spectroscopy (XAS) [26], small-angle X-ray scattering (SAXS) [18,20], and computer simulations [27–35]. Most of these studies have been on model binary, ternary and quaternary Fe–Cu-based carbon-free alloys and low-carbon steels. Fewer studies exist on Cu precipitation in multicomponent steels with increased alloying concentrations and microstructural complexity. The recent studies of Vaynman et al. [1] and Isheim et al. [36–38] characterized the Cu-rich precipitates found within multicomponent Fe–Cu-based steels. The precipitates were studied at near-peak hardness and in the slightly over-aged condition.

Studies of growth and coarsening (Ostwald ripening) of the Cu precipitates are likewise few in number. Speich and Oriani [14] studied coarsening in binary Fe–Cu alloys containing 2.3–5.4 wt.% Cu, at aging temperatures between 730 and 830 °C. These authors reported that the kinetics obey the $t^{1/3}$ power-law law for mean radius, $\langle R(t)\rangle$, predicted by the Lifshitz–Slyzov–Wagner (LSW) [39,40] model for coarsening, see below. Monzen et al. [41,42] studied an Fe–1.5 wt.% Cu alloy at temperatures between 600 and

* Corresponding author. Tel.: +1 630 305 2386; fax: +1 630 305 2921.
E-mail addresses: rpkolli@nalco.com (R. Prakash Kolli), d-seidman@northwestern.edu (D.N. Seidman).

1359-6454/$34.00 © 2008 Acta Materialia Inc. Published by Elsevier Ltd. All rights reserved.
doi:10.1016/j.actamat.2007.12.044

750 °C and also reported good agreement with the $t^{1/3}$ power-law for $\langle R(t)\rangle$. These authors also reported that the kinetics of the matrix supersaturation, followed using electrical resistivity measurements, obey the $t^{-1/3}$ power-law, as predicted by the LSW model. Soisson et al. [27] studied, by lattice kinetic Monte Carlo simulations, a binary Fe–1.34 at.% Cu alloy aged between 300 and 500 °C; they reported a $t^{1/3}$ dependency for $\langle R(t)\rangle$. Recently, investigations by Isheim et al. [37] described the temporal evolution of $\langle R(t)\rangle$, number density, $N_V(t)$, and concentration profiles for a multicomponent Fe–Cu-based steel.

The LSW model describes mean-field diffusion-limited coarsening of precipitates in dilute binary alloys [43,44]. The asymptotic solutions of the LSW model [39,40] predict:

$$\langle R(t)\rangle - \langle R(t_0)\rangle \propto t^{1/3}, \tag{1}$$

where t is time and $\langle R(t_0)\rangle$ is the mean radius at the onset of quasi-stationary coarsening, where t_0 is greater than zero. The model also predicts:

$$N_V(t) - N_V(t_0) \propto t^{-1}, \tag{2}$$

where $N_V(t_0)$ is the number density at the onset of coarsening, and:

$$\Delta C_i^{\text{mat.}}(t) = |[\langle C_i^{\text{mat.,ff}}(t)\rangle - C_i^{\text{mat.,eq.}}(\infty)]| \propto t^{-1/3}; \tag{3}$$

where $\Delta C_i^{\text{mat.}}(t)$ is the matrix (mat.) supersaturation of an element i at time t between the far-field concentration of element i, $\langle C_i^{\text{mat.,ff}}(t)\rangle$, and equilibrium concentration, $C_i^{\text{mat.,eq.}}(\infty)$. The assumptions of the LSW model are: (1) the linearized Gibbs–Thompson equation is valid; (2) the precipitate volume fraction is essentially zero; (3) the diffusion fields of the precipitates do not overlap; (4) dilute solution theory applies; (5) no elastic interactions occur among the precipitates; (6) the precipitates have a spherical morphology; (7) the precipitates form and coarsen with the composition given by the equilibrium phase diagram; (8) the evaporation–condensation mechanism is implicit in the model; and (9) the system is in the stationary state, which is obtained from the asymptotic solutions at infinite time. The Umantsev–Olson (UO) model [45] extends the LSW model from binary to multicomponent alloys, employing the same assumptions excluding that the alloy is a dilute solution and the precipitating phase has a volume fraction of zero. It predicts the same time exponents as the LSW model albeit with different rate constants. And, finally, Kuehmann and Voorhees (KV) [46] have analyzed ternary alloys in significantly greater detail.

The focus of this investigation is the nucleation (to a limited extent), growth and coarsening of the Cu-rich precipitates in a concentrated multicomponent Fe–Cu-based steel containing 1.82 at.% Cu. This steel is being studied as part of a program to develop an explosion-resistant steel for the US Navy [1,47,48]. The temporal evolution of the morphologies and compositions of the Cu-rich precipitates, from the as-quenched condition to 1024 h, when aged at 500 °C, is studied utilizing APT [49]. We discuss the temporal evolution of the precipitate core and precipitate/α-Fe matrix heterophase interface compositions in detail. The power-law time exponents are experimentally determined for $\langle R(t)\rangle$, $N_V(t)$ and $\Delta C_i^{\text{mat.}}(t)$. Additionally, we determine the exponents for the precipitate (ppt.) core, $\Delta C_i^{\text{ppt.}}(t) = |[\langle C_i^{\text{ppt.}}(t)\rangle - C_i^{\text{ppt.,eq.}}(\infty)]|$, and heterophase interfacial region (int.), $\Delta C_i^{\text{int.}}(t) = |[\langle C_i^{\text{int.}}(t)\rangle - C_i^{\text{int.,eq.}}(\infty)]|$, supersaturations of an element i at time t, where $C_i^j(t)$ is the concentration as a function of time and $C_i^{j.\text{eq.}}(\infty)$ is the equilibrium concentration for phase j (j = mat., ppt., or int.). The results obtained are compared to predictions of the UO model [45] and to earlier investigations for coarsening in binary Fe–Cu alloys [14,27,41,42]. Furthermore, we discuss the equilibrium morphology of the precipitates and delineate the formation of a Ni–Al–Mn phase at the Cu-rich precipitate and α-Fe matrix interfaces.

2. Experimental methods

2.1. Material details

A 45.5 kg (100 lb) steel heat was vacuum induction melted and cast at ArcelorMittal Steel Global Research & Development, East Chicago, IN. The heat was reheated to approximately 1150 °C and hot-rolled in multiple passes to a thickness of 12.5 mm and then air-cooled to room temperature. The final hot-rolling temperature was approximately 900 °C. The bulk composition of the steel, determined by spectrographic analysis at ArcelorMittal Steel Global Research & Development, is presented in Table 1. We denote this steel NUCu-170[1] (170 designates the yield strength in ksi); details regarding the development of the NUCu series of steels can be found in Ref. [1]. The plates were trimmed and cut into rods 12.5 × 12.5 mm × 250 mm and solutionized at 900 °C for 1 h and then quenched into water at 25 °C. Material (12.5 mm × 12.5 mm × 25 mm blocks) for hardness testing and APT were aged at 500 °C for 0.25, 1, 4, 16, 64, 256 or 1024 h and subsequently quenched into water at 25 °C.

2.2. Vickers microhardness

Sections were cold mounted in acrylic and polished utilizing standard metallographic procedures to a final surface finish of 1 μm for hardness testing. Hardness testing was performed in accordance with ASTM standards (ASTM E 384-99) using a Buehler Micromet II microhardness tester with a Vickers microhardness indenter, a load of 500 g and a testing time of 15 s. The reported microhardness values are derived from 10 measurements on each specimen.

[1] The term NUCu stands for Northwestern University copper alloyed steel.

Table 1
Nominal composition of high-strength low-carbon Fe–Cu-based steel

	Cu	C	Al	Ni	Si	Mn	Nb	P	S
wt.%	2.09	0.045	0.68	2.83	0.51	0.50	0.065	0.010	0.003
at.%	1.82	0.209	1.38	2.67	1.00	0.51	0.038	0.018	0.005

Balance is Fe.

2.3. Atom-probe tomography

The steel blocks were further reduced to 0.3 mm × 12.5 mm × 25 mm coupons, cut from the center, utilizing an abrasive saw. The APT tip blanks (0.3 mm × 0.3 mm × 25 mm) were mechanically cut from the coupons and electropolished using standard techniques [49,50]. Initial polishing was performed with a solution of 10 vol.% perchloric acid in acetic acid at 15–10 V DC at room temperature. This was followed by a manually controlled pulsed final-polishing step using a solution of 2 vol.% perchloric acid in butoxyethanol at 10–5 V DC at room temperature, producing a tip with a radius <50 nm. LEAP™ tomography [51,52] was performed at a specimen temperature of 50 K under ultrahigh vacuum (UHV) conditions of $\sim 1 \times 10^{-8}$ Pa ($\sim 7.5 \times 10^{-11}$ torr). The pulse repetition rate was 2×10^5 Hz and the pulse-voltage-to-standing-DC voltage ratio (pulse fraction) was 15–20%.

Visualization and reconstruction of the APT data is performed using the Imago Visualization and Analysis Software (IVAS™) package. The precipitates are identified utilizing an isoconcentration surface methodology [53] with the threshold concentration set at 10 at.% Cu, which gives morphologically and compositionally stable results. The parameters chosen to obtain noise-free isoconcentration surfaces are a voxel size of 1 nm, a delocalization distance of 4 nm, a sample count threshold of 5%, and a polygon filter level of 10–20.

Concentration profiles with respect to distance from the reference isoconcentration surfaces are obtained utilizing the proximity histogram (proxigram for short) with a bin width of 0.25 nm [54]. The $\pm 2\sigma$ standard deviations for the reported concentrations are given by counting statistics:

$$\sigma = \sqrt{\frac{c_i(1-c_i)}{N_{\mathrm{TOT}}}}, \tag{4}$$

where c_i is the atomic fraction of an element i in a bin and N_{TOT} is the total number of ions in a bin.

The spherical volume equivalent radius, R, of a precipitate [55] is given by:

$$R = \left(\frac{3}{4\pi}\frac{N_{\mathrm{atoms}}}{\rho_{\mathrm{th}}\eta}\right)^{\frac{1}{3}}, \tag{5}$$

where N_{atoms} is the number of atoms detected within a delineated precipitate, ρ_{th}, is the theoretical atomic density, which is equal to 84.3 atoms nm^{-3} for this steel, and η is the estimated detection efficiency of 0.5 of the multichannel plate detector. The value of N_{atoms} belonging to a precipitate is determined from the envelope method [49,56], based on a maximum separation distance, $d_{\max}$, of 0.5–0.6 nm, a minimum number of solute atoms, $N_{\min}$, of 11–100 Cu atoms (depending on the aging time), and a grid spacing of 0.2 nm. The details regarding selection of values for the parameters utilized in the envelope method for this steel can be found in Ref. [55].

The radial distribution function (RDF) [57], with respect to Cu for this steel, is defined as the average concentration of an element i at a distance r from the Cu atoms, $\langle C_i^{\mathrm{Cu}}(r)\rangle$, normalized to the overall concentration of the element i, C_i^{o}, in the alloy:

$$\mathrm{RDF} = \frac{\langle C_i^{\mathrm{Cu}}(r)\rangle}{C_i^{\mathrm{o}}} = \frac{1}{C_i^{\mathrm{o}}}\sum_{k=1}^{N_{\mathrm{Cu}}}\frac{N_i^k(r)}{N_{\mathrm{tot}}^k(r)}, \tag{6}$$

where $N_i^k(r)$ is the number of i atoms in a radial shell around the kth Cu atom at a distance r, and $N_{\mathrm{tot}}^k(r)$ is the total number of atoms within the shell at a distance r. The partial RDFs are calculated using 0.01 nm increments from 0.2 to 1.0 nm. Only the partial RDFs for $r \geqslant 0.2$ nm are displayed, as the physical interpretation at smaller r values is difficult due to possible ion trajectory effects. The results are smoothed by a weighted moving average using a Gaussian-type spline function [53]. Radial distribution function values >1 imply a positive correlation with Cu atoms, whereas values <1 imply a negative correlation with Cu atoms. A value of unity indicates a random distribution of element i with respect to Cu. Greater detail regarding the RDF can be found in Refs. [57,58]. The partial RDF is utilized to evaluate any potential clustering, in the as-quenched specimen, with a greater degree of sensitivity than the isoconcentration surface [53] or envelope [49,56] methodologies.

2.4. Transmission electron microscopy

Specimens for conventional transmission electron microscopy (TEM) were mechanically cut from the 0.3 mm × 12.3 mm × 25 mm coupons aged for 1024 h. The 3 mm foils were then mechanically ground to a thickness of approximately 150 μm and subsequently twin-jet electropolished in a solution of 5 vol.% perchloric acid in methanol at −60 °C and 15 V. The specimen perforations were further thinned utilizing ion-beam thinning (IBT) at 3.0 kV and 3.5 mA. The specimens were examined in a Hitachi H-8100 transmission electron microscope operating at 200 kV.

3. Results

3.1. Temporal evolution of the morphology

Fig. 1 displays the Vickers microhardness (VHN) as function of aging time. This figure demonstrates that a significant increase in hardness is attainable when the steel is

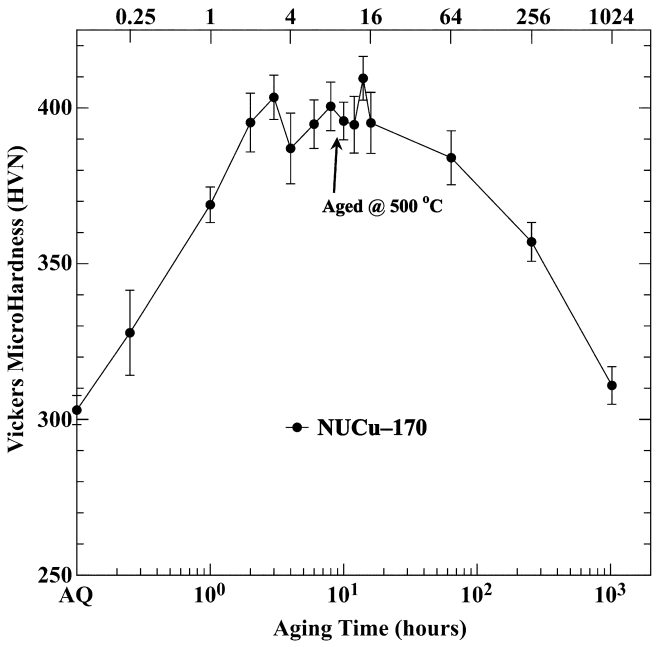

Fig. 1. Vickers microhardness (VHN) as a function of aging time (h) when the NUCu-170 steel is aged at 500 °C. A plateau of ~395 VHN is seen between 2 and 16 h.

aged at 500 °C. Prior to 2 h of aging the steel is under-aged. From 2 to 16 h of aging the microhardness reaches a plateau of approximately 395 VHN. The observed hardness plateau is a result of different nucleation and growth rates of the Cu-rich and NbC precipitates [59,60] present within the steel and is consistent with earlier observations on NUCu steels containing ~1.13–1.20 at.% Cu [1]. At 64 h of aging the microhardness decreases to 384.0 ± 8.7 VHN, indicating the steel is over-aged. Aging for times greater than 64 h results in further reduction of hardness, reaching a value of 310.9 ± 6.1 VHN at 1024 h. Other researchers have reported aging times ranging from 1.94 to ~10 h to achieve peak hardness in model Fe–Cu-based alloys containing between 1.1 and 1.5 at.%. Cu, when aged at 500 °C [7,10,12,13,20,24,30,61,62].

Evolution of the Cu-rich precipitate morphology is seen qualitatively in Fig. 2a–g, which depict $10 \times 10 \times 30$ nm^3 (3000 nm^3) subsets of an analyzed volume for each aging time studied, containing approximately 130,000 atoms. These figures illustrate that the precipitates, which are delineated with 10 at.% Cu isoconcentration surfaces, grow and coarsen with increasing aging time. The precipitates are initially spheroidal and become more ellipsoidal or rod-like at 1024 h of aging, although, as discussed below, not all precipitates at 1024 h have a rod-like morphology.

A representative Cu-rich precipitate for a 1 h aging time is presented in Fig. 3a. In Fig. 3a–c the Cu atoms are orange,[2] the Ni atoms are green, the Al atoms are teal, the Mn atoms are mustard, and the Fe atoms are blue,

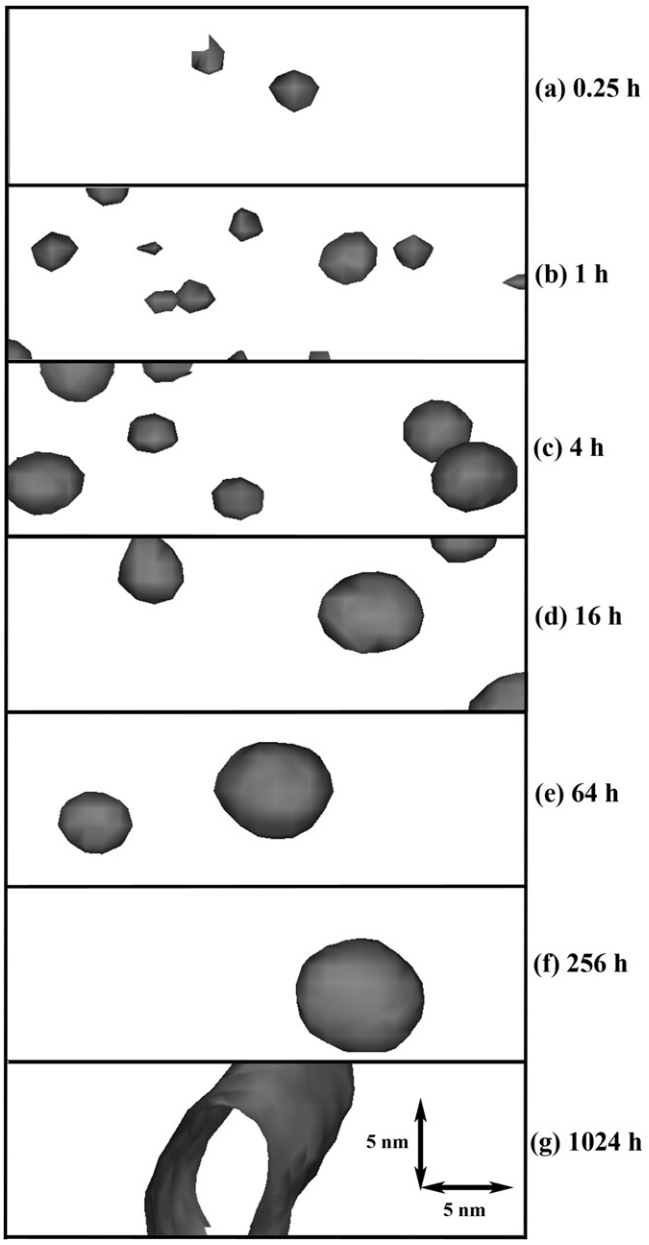

Fig. 2. Copper-rich precipitates as delineated by 10 at.% Cu isoconcentration surfaces, when the steel is aged at 500 °C for: (a) 0.25 h; (b) 1 h; (c) 4 h; (d) 16 h; (e) 64 h; (f) 256 h; (g) 1024 h. Each reconstruction, $10 \times 10 \times 30$ nm^3 (3000 nm^3), is a subset of an analyzed volume and contains approximately 130,000 atoms.

and the Si atoms are gray. The distribution of Ni, Al and Mn atoms adjacent to the Cu atoms, at the precipitate/α-Fe matrix heterophase interface, is illustrated. The segregation is more pronounced on one side of the precipitate. Other precipitates for this aging time exhibit similar segregation and this observation is consistent with previously reported results in similar concentrated multicomponent steels [36–38]. A representative precipitate for the 4 h aging time is displayed in Fig. 3b. The observed Ni, Al and Mn segregation is similar to that observed at 1 h, which is discussed in detail below. We observe similar segregation behavior for Ni, Al and Mn in other precipitates at this

[2] For interpretation to color in Fig. 3, the reader is referred to the web version of this article.

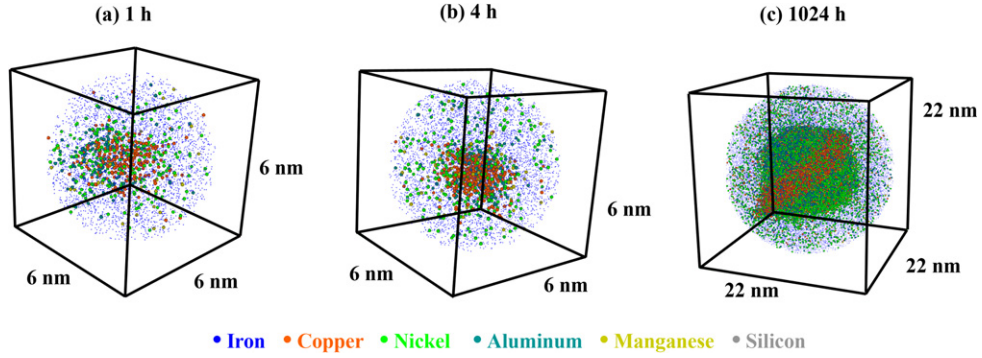

Fig. 3. Three-dimensional atom-probe tomographic reconstructions of representative precipitates in the (a) 1 h, (b) 4 h and (c) 1024 h aged conditions. The precipitate presented in (c) is of rod-like morphology. The Cu, Ni, Al and Mn atoms are shown as spheres (not to scale), allowing visualization of the precipitates and heterophase interfaces. Only 20% of the Fe and 50% of the Cu, Ni, Al, and Mn atoms are shown in (c) for clarity.

aging state. The precipitate displayed in Fig. 2g, 1024 h of aging, is larger than the cross-sectional area employed, and extends beyond the boundaries of the volume displayed. The exact same precipitate is presented in Fig. 3c. The precipitate has a rod-like morphology consisting almost entirely of Cu atoms in its core and is partially surrounded by Ni, Al and Mn atoms, where the observed segregation is greater qualitatively than for the 4 h aged state, see below. The segregation of the elements Ni, Al and Mn is not uniform around the Cu atoms in the core of the precipitate. Unlike for the 1 and 4 h aging conditions, the observed segregation occurs predominantly on two sides of this precipitate. Not all precipitates at this aging time possess the same morphology presented in Figs. 2g and 3c. Other precipitates exhibit a more spheroidal morphology with Ni, Al and Mn segregating toward one side of the Cu-rich core (Fig. 4).

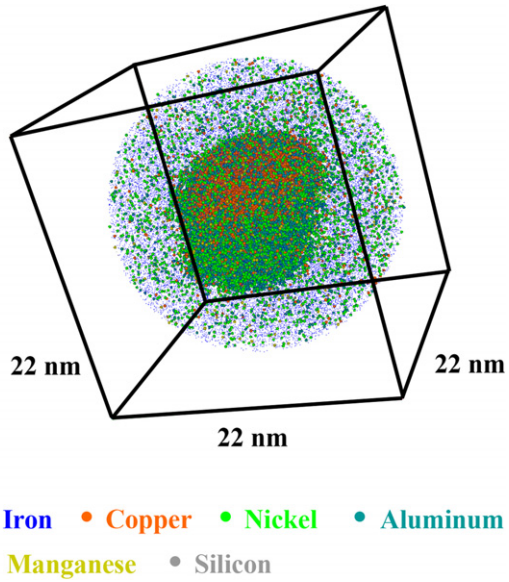

Fig. 4. Three-dimensional atom-probe tomographic reconstruction of a spheroidal shaped precipitate found in the 1024 h aged condition. The Cu, Ni, Al and Mn atoms are shown as spheres (not to scale) allowing visualization of the precipitates and heterophase interfaces. Only 20% of the Fe and 50% of the Cu, Ni, Al and Mn atoms are shown for clarity.

3.1.1. Nucleation and growth

We do not find any evidence of precipitation within the matrix in the as-quenched state utilizing the isoconcentration surface methodology [53] with the designated parameters. Reduction of the threshold concentration to values as small as the bulk Cu concentration does not affect the observed result. We also do not find any evidence of precipitation utilizing the envelope method [49,56] with the designated parameters and the methodology described in Ref. [55]. The steel, when in the supersaturated state, exhibits some evidence of forming metastable clusters (embryos). Utilizing the same value for d_{max} and setting $N_{min} = 3$ Cu atoms gives 813 clusters (embryos) containing 3–20 Cu atoms. The majority of clusters (embryos), 801, contain less than 11 Cu atoms, suggesting they are metastable clusters (embryos). The larger agglomerations are possibly stable clusters, i.e. early-stage stable nuclei.

To further evaluate this steel in the as-quenched state, an experimental partial RDF, determined by Eq. (6) and presented in Fig. 5a–f, is utilized. The 1st–6th nearest-neighbor (NN) distances and NN numbers for body-centered cubic (bcc) α-Fe are given on the top abscissa. These figures illustrate that strong overall positive correlations exist for Cu–Cu (Fig. 5a), Cu–Al (Fig. 5d) and Cu–Si (Fig. 5f) atoms, whereas a strong negative correlation exists for Cu–Mn (Fig. 5e) atoms. The strong positive oscillation for Cu–Cu between the second and third NN positions along with the results of the envelope method suggests that the onset of phase decomposition may occur as early as after solutionizing and quenching to room temperature. The slight negative oscillation for Cu–Fe (Fig. 5b) is a minimum between the first and second NN positions, suggesting that Cu and Fe are negatively correlated at this location. However, the closeness of the partial RDF to unity indicates that Fe is almost randomly distributed relative to Cu. The Cu–Ni partial RDF (Fig. 5c) demonstrates a weak overall negative correlation but the proximity of the partial RDF to unity between the first and second NN positions suggests a random distribution of Ni with respect to Cu.

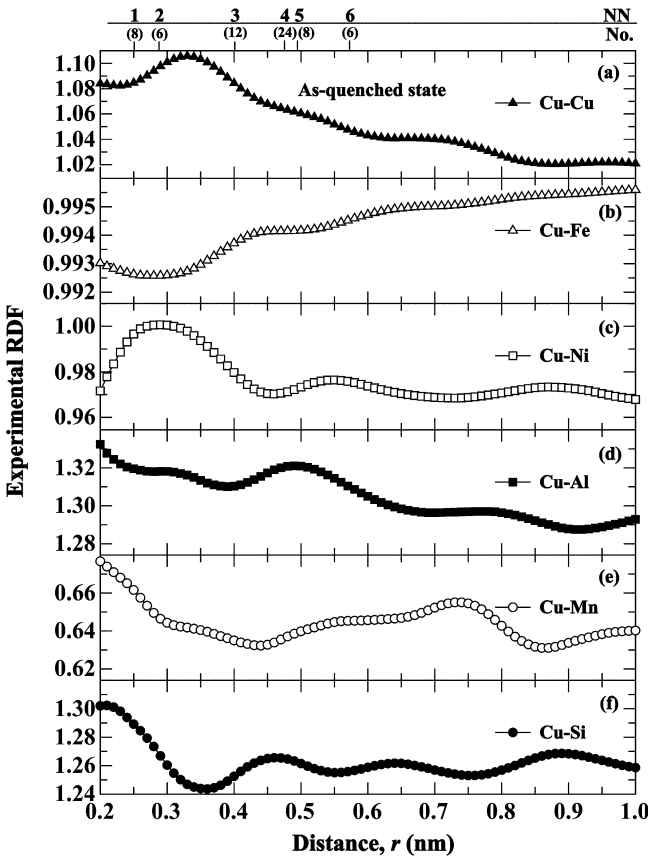

Fig. 5. Experimental partial radial distribution function (RDF) in the as-quenched state for: (a) Cu–Cu atoms; (b) Cu–Fe atoms; (c) Cu–Ni atoms; (d) Cu–Al atoms; (e) Cu–Mn atoms; and (f) Cu–Si atoms. Values of RDF >1 indicate a positive correlation between atoms, whereas values of RDF < 1 indicate a negative correlation between atoms; when the RDF = 1 this indicates a random distribution. The 1st–6th nearest neighbor (NN) distances and NN numbers for bcc Fe are indicated on the top abscissa.

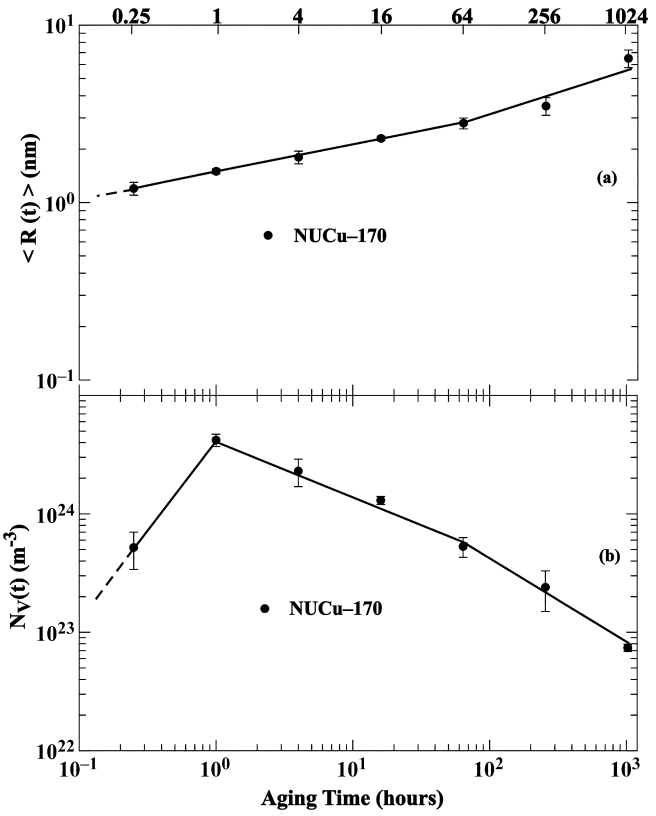

Fig. 6. The (a) mean precipitate radius, $\langle R(t)\rangle$; and (b) number density, $N_V(t)$, as a function of aging time for an aging temperature of 500 °C.

By 0.25 h, Cu-rich precipitates have formed within the matrix (Fig. 2a) with $\langle R\rangle = 1.2 \pm 0.1$ nm (Fig. 6a), where the error is given by standard error of the mean. At 0.25 h, $N_V = (5.2 \pm 1.8) \times 10^{23}\ m^{-3}$ (Fig. 6b) and the volume fraction, ϕ, is equal to $0.3 \pm 0.01\%$, where the reported error is based on counting statistics for both quantities. Further aging to 1 h results in a significant increase of $N_V(t)$ to $(4.2 \pm 0.5) \times 10^{24}\ m^{-3}$, with $\langle R\rangle = 1.5 \pm 0.05$ nm, and ϕ equal to $3.6 \pm 0.06\%$. The increase in $N_V(t)$ occurs with a temporal dependency of $t^{2.7}$, in conjunction with a time exponent for $\langle R(t)\rangle$ equal to 0.16, indicating that nucleation is occurring. The slowly increasing value of $\langle R(t)\rangle$ indicates, however, that growth is also occurring simultaneously.

3.1.2. Growth and coarsening

The quantity $N_V(t)$ reaches a maximum at 1 h of aging and subsequently decreases indicating the onset of coarsening. The value of $\langle R(t)\rangle$ increases from 1.5 ± 0.05 nm at 1 h to 6.5 ± 0.7 nm at 1024 h (Fig. 6a) and the temporal dependencies for $\langle R(t)\rangle$ are $t^{0.16\pm0.01}$ from 1 to 64 h and $t^{0.34\pm0.09}$ from 64 to 1024 h. Only from 64 h onwards is the time exponent equal to that predicted by Eq. (1). The quantity $N_V(t)$ decreases by a factor of 56 to $(7.4 \pm 0.5) \times 10^{22}\ m^{-3}$ at 1024 h with ϕ equal to $4.3 \pm 0.06\%$. The temporal dependencies for $N_V(t)$ are $t^{-0.45\pm0.03}$ from 1 to 64 h and $t^{-0.63\pm0.07}$ from 64 to 1024 h, which indicates coarsening is occurring slower than that predicted by Eq. (2).

3.2. Temporal evolution of composition

The temporal evolution of the concentration profiles is presented in Figs. 7 and 8a–c. The figures represent the temporal evolution of the Cu, Fe, Ni, Al, Mn and Si profiles from the under-aged condition, 0.25 h (Fig. 7) and 1 h (Fig. 8a), to the peak yield strength aged condition, 4 h (Fig. 8b), and finally to the over-aged condition at 1024 h (Fig. 8c). These figures demonstrate clearly that the composition of the matrix, precipitates and precipitate/α-Fe matrix heterophase interfaces are evolving temporally. The observed segregation of Ni, Al and Mn is non-monotonic (confined), whereas the observed segregation of Cu, Fe and Si is monotonic (non-confined).

3.2.1. Far-field matrix compositions

In this investigation the plateau points [63] within the matrix (far-field) yield the α-Fe matrix concentrations (Table 2), where the plateau region of the proxigram is

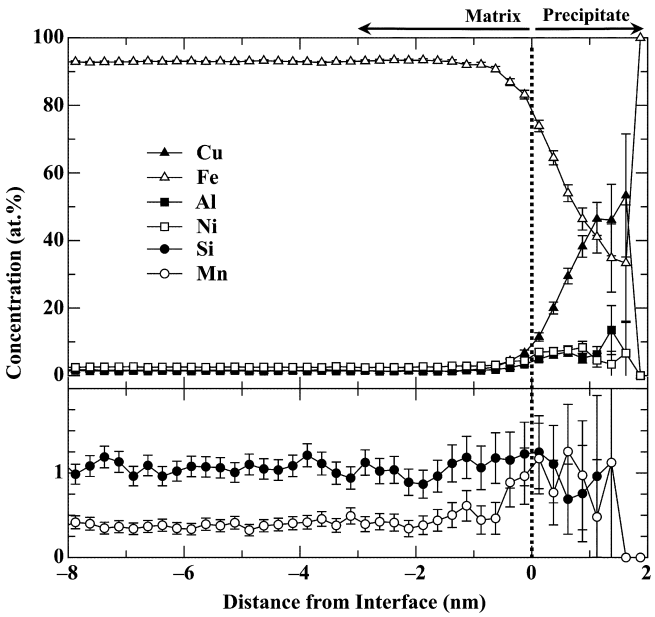

Fig. 7. Proxigram concentration profiles (at.%) for Cu, Fe, Al, Si and Mn, when the steel is aged at 500 °C for 0.25 h. The dotted vertical line corresponds to the α-Fe matrix/precipitate heterophase interface.

delineated by utilizing the Fe concentration profiles as a fiducial marker. Only data points within the flat region of the profile, a minimum of 1.5 nm away from the hetero-phase interface and with $\pm 2\sigma < 0.4$ at.%, are included. The concentration of Cu decreases in the α-Fe matrix, reaching a value of 0.2 ± 0.01 at.% at 1024 h of aging. The concentrations of Ni, Al and Mn in the α-Fe matrix also decrease with prolonged aging time. The concentrations of Si and Fe increase in the α-Fe matrix with increasing aging time, which becomes enriched in these elements at 1024 h. Niobium is not detected within the α-Fe matrix, with the exception of the 1 h aged state, while C is detected at a reduced concentration when compared to its nominal value. In the NUCu steels Nb is not normally detected by APT due to the existence of NbC precipitates at a smaller number density ($\leqslant 10^{22}$ m^{-3}) than the Cu-rich precipitates [1,59,60]. In the 1 h aged state the presence of a single NbC precipitate at the boundary of an analyzed volume gives the measured Nb concentration. Similarly, C is detected at lower concentrations within the matrix due to the presence of NbC precipitates, cementite (Fe_3C) [37] and segregation at grain boundaries [37].

3.2.2. Composition of the Cu-rich precipitates

At 0.25 h of aging the precipitate cores are Cu-rich (46.7 ± 4.3 at.%) but also contain significant concentrations of Fe, Ni and Al, and smaller quantities of Si and Mn (Table 3). At 1 h of aging the precipitate cores are also Cu-rich (44.6 ± 3.1 at.%) but still contain significant

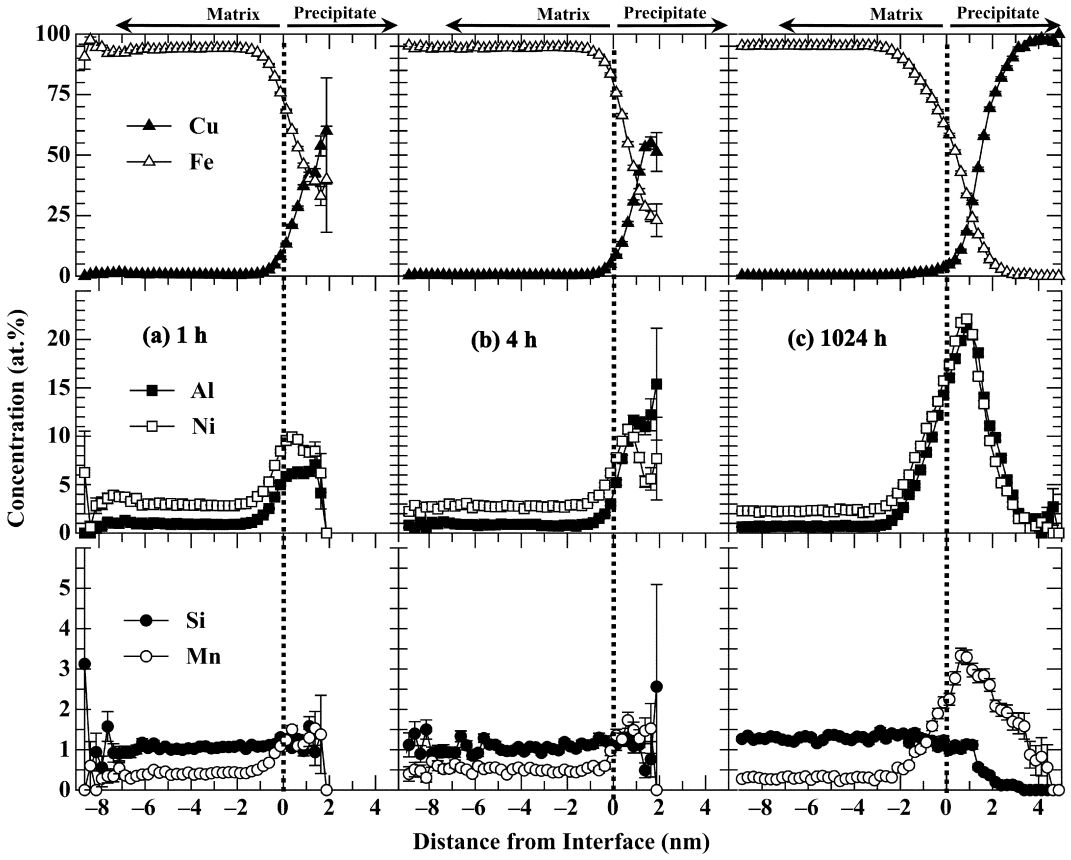

Fig. 8. Proxigram concentration profiles (at.%) for Cu, Fe, Ni, Al, Si and Mn, when the steel is aged at 500 °C, for (a) 1 h, (b) 4 h and (c) 1024 h. The dotted vertical lines indicate the α-Fe matrix/precipitate heterophase interface.

Table 2
Composition in at.% of the α-Fe matrix of the specimens aged at 500 °C as determined by atom-probe tomography

	Cu	C	Al	Ni	Si	Mn	Fe	Nb
0.25 h	1.6 ± 0.02	0.04 ± 0.004	1.4 ± 0.02	2.6 ± 0.03	1.1 ± 0.01	0.4 ± 0.01	92.9 ± 0.01	ND
1 h	0.6 ± 0.01	0.06 ± 0.004	0.9 ± 0.02	2.9 ± 0.03	1.1 ± 0.02	0.4 ± 0.01	93.8 ± 0.04	0.007 ± 0.001
4 h	0.4 ± 0.07	ND	0.8 ± 0.2	2.8 ± 0.4	1.0 ± 0.2	0.5 ± 0.2	94.4 ± 0.5	ND
16 h	0.5 ± 0.2	0.05 ± 0.05	0.9 ± 0.2	2.6 ± 0.4	1.2 ± 0.2	0.3 ± 0.1	94.4 ± 0.5	ND
64 h	0.3 ± 0.3	0.01 ± 0.01	0.8 ± 0.5	2.0 ± 0.7	1.1 ± 0.6	0.4 ± 0.3	95.4 ± 1.1	ND
256 h	0.3 ± 0.1	0.008 ± 0.002	0.7 ± 0.2	2.4 ± 0.3	1.3 ± 0.2	0.4 ± 0.1	94.9 ± 0.5	ND
1024 h	0.2 ± 0.01	0.03 ± 0.002	0.7 ± 0.01	2.3 ± 0.02	1.3 ± 0.02	0.3 ± 0.01	95.1 ± 0.04	ND

ND = Not detected.

Table 3
Composition in at.% of the Cu-rich precipitate cores of the specimens aged at 500 °C as determined by atom-probe tomography

	Cu	C	Al	Ni	Si	Mn	Fe	Nb
0.25 h	46.7 ± 4.3	0.2 ± 0.2	7.4 ± 2.2	4.5 ± 1.8	0.9 ± 0.8	0.6 ± 0.6	39.9 ± 4.2	ND
1 h	44.6 ± 3.1	0.1 ± 0.1	6.6 ± 1.7	8.1 ± 1.7	1.0 ± 0.6	1.5 ± 0.8	38.3 ± 3.1	ND
4 h	53.5 ± 2.3	ND	11.3 ± 1.5	5.4 ± 1.1	0.6 ± 0.4	1.5 ± 0.6	27.6 ± 2.1	ND
16 h	66.0 ± 1.8	ND	9.8 ± 1.1	14.8 ± 1.4	0.4 ± 0.3	1.1 ± 0.4	14.8 ± 1.4	ND
64 h	88.4 ± 1.7	ND	1.6 ± 0.7	2.5 ± 0.8	0.1 ± 0.1	1.1 ± 0.6	6.3 ± 1.3	ND
256 h	78.3 ± 3.0	0.1 ± 0.1	4.7 ± 1.5	8.9 ± 2.0	0.1 ± 0.1	2.3 ± 1.1	5.5 ± 1.6	ND
1024 h	97.1 ± 0.8	ND	1.2 ± 0.4	0.7 ± 0.4	0	0.8 ± 0.4	0.3 ± 0.2	ND

ND = Not detected.

amounts of Fe, Ni, Al, Mn and Si. As aging progresses, the Cu concentration within the cores increases to 53.5 ± 2.3 at.% at 4 h and achieves a value of 97.1 ± 0.8 at.% at 1024 h. Concomitantly, the concentrations of Fe and Si decrease, reaching a value of 0.3 ± 0.2 at.% and zero, respectively, at 1024 h. The concentrations of Ni, Al and Mn within the cores have a more complicated behavior, which is discussed below. Prior to 1024 h, however, all three elements are found enhanced within the cores at the aging times studied. At 1024 h the cores are depleted in Ni (0.7 ± 0.4 at.%) and Al (1.2 ± 0.4 at.%), relative to their nominal concentrations, whereas Mn is enriched (0.8 ± 0.4 at.%). Carbon and Nb are not found within the precipitate cores, within the prescribed experimental uncertainty.

3.2.3. Composition of precipitate/α-Fe matrix heterophase interfaces

The composition of the precipitate/α-Fe matrix heterophase interfaces is also illustrated in Figs. 7 and 8a–c. The heterophase interfacial region, at as early as 0.25 h of aging, is enriched in Cu, Ni, Al and Mn but is depleted in Fe (Table 4). The Ni peak concentration (8.3 ± 1.8 at.%) is located at a distance of 0.875 nm close to the Mn peak concentration (1.3 ± 0.5 at.%), which is found at a distance of 0.625 nm. The Al peak concentration (13.5 ± 7.2 at.%) is located toward the center of the precipitate at 1.375 nm. At 1 h, the Ni (9.9 ± 0.5 at.%) and Mn (1.5 ± 0.2 at.%) peak concentrations are located at a distance of 0.375 nm, whereas the Al peak concentration (7.1 ± 1.7 at.%) is found closer to the center of the precipitate at a distance of 1.375 nm. At 4 h the Ni (10.7 ± 0.3 at.%) and Mn (1.7 ± 0.4 at.%) peak concentrations are co-located at a distance of 0.625 nm, while the Al peak concentration (12.2 ± 3.2 at.%) is at a distance of 1.625 nm. At 1024 h of aging a distinct enhancement of Ni, Al and Mn is observed at the heterophase interfaces, with peak concentrations of 22.1 ± 0.8 at.% Ni and 21.2 ± 0.8 at.% Al at a distance of 0.875 nm and 3.3 ± 0.3 at.% Mn at a distance of 0.625–0.875 nm. The evolution of the Ni, Al and Mn concentrations within the heterophase interfaces is related to that within the precipitate cores and is discussed below.

Table 4
Composition in at.% of the precipitate/α-Fe matrix heterophase interfaces of the specimens aged at 500 °C as determined by atom-probe tomography

	Cu	C	Al	Ni	Si	Mn	Fe	Nb
0.25 h	3.3 ± 0.1	0.05 ± 0.01	1.9 ± 0.08	3.1 ± 0.1	1.0 ± 0.06	0.5 ± 0.04	90.1 ± 0.04	ND
1 h	5.0 ± 0.08	0.08 ± 0.01	2.5 ± 0.05	5.1 ± 0.07	1.1 ± 0.03	0.7 ± 0.03	85.1 ± 0.1	0.009 ± 0.003
4 h	6.2 ± 0.2	ND	3.2 ± 0.1	5.1 ± 0.1	1.2 ± 0.07	0.8 ± 0.06	83.4 ± 0.3	ND
16 h	8.7 ± 0.05	0.05 ± 0.004	5.2 ± 0.04	6.9 ± 0.05	1.2 ± 0.02	0.7 ± 0.02	77.1 ± 0.07	ND
64 h	8.4 ± 0.06	0.02 ± 0.003	4.8 ± 0.05	6.1 ± 0.05	1.1 ± 0.02	0.9 ± 0.02	78.5 ± 0.09	ND
256 h	10.4 ± 0.1	0.01 ± 0.004	6.6 ± 0.09	8.5 ± 0.1	1.3 ± 0.04	1.1 ± 0.04	72.0 ± 0.2	ND
1024 h	10.3 ± 0.08	0.04 ± 0.005	5.2 ± 0.06	6.5 ± 0.07	1.2 ± 0.03	1.0 ± 0.03	75.7 ± 0.1	ND

ND = Not detected.

Silicon is also found within the heterophase interfacial region at a slightly enhanced concentration of approximately 1.1–1.3 at.%. Niobium is not detected, with the exception of the 1 h aged condition, while C is detected at a reduced concentration when compared to its nominal value.

3.2.4. Partitioning ratios

The temporal evolution of the partitioning ratio [55],

$$\kappa_i^{\mathrm{ppt./mat.}}(t) = C_i^{\mathrm{ppt.}}(t)/C_i^{\mathrm{mat.,ff}}(t), \tag{7}$$

is displayed in Fig. 9. The standard error for κ_i is determined by standard error propagation methods for the concentration errors [64]. This figure illustrates clearly that Cu partitions to the precipitates, whereas Fe and Si partition to the matrix. The dashed line, beyond 256 h, for the Si ratio, represents the zero Si concentration within the precipitate core at 1024 h of aging. Nickel, Al and Mn exhibit a more complicated behavior but slightly prefer the Cu-rich precipitate phase from 0.25 to 256 h. At 1024 h Fig. 9 shows that Al and Mn have a slight preference for the precipitate, whereas Ni has a slight preference for the α-Fe matrix. The proximity of all three elements, though, to the dashed line separating precipitate and matrix phases indicates that the three elements partition to the interfacial region. The partitioning ratios for Ni and Mn exhibit similar trends from 0.25 to 16 h, where they diverge slightly, whereas the profiles of Ni and Al follow similar trends from 64 to 1024 h.

3.2.5. Coarsening kinetics

The matrix, precipitate core and precipitate/α-Fe matrix heterophase interface supersaturations are displayed in Figs. 10–12. The equilibrium concentrations are obtained by extrapolating the concentration of each element as a function of (aging time)$^{-1/3}$ to infinite time, analogous to the procedure found in Ref. [65]. The experimentally determined equilibrium concentration values, the concentrations measured at 1024 h of aging, and those predicted by Thermo-Calc are displayed in Table 5. The time exponents for $\Delta C_i^{\mathrm{mat.}}(t)$ (Fig. 10a–c) are -0.23 ± 0.07 for Cu, -0.32 ± 0.06 for Fe, -0.25 ± 0.03 for Ni, -0.22 ± 0.09 for Al, -0.14 ± 0.14 for Mn, and -0.25 ± 0.13 for Si. The time exponents for all elements, except Si, are derived from aging times of 1 to 1024 h, while that of Si is from 1 to 64 h, since $\Delta C_i^{\mathrm{mat.}}(t) = 0$ at.%, is reached at 256 h for Si. The time exponents for $\Delta C_i^{\mathrm{ppt.}}(t)$ (Fig. 11a–c) are -0.26 ± 0.06 for Cu, -0.37 ± 0.04 for Fe and -0.41 ± 0.05 for Si. The exponents for Cu and Fe are derived for aging times of 1–1024 h, while the exponent for Si is for aging times of 1–256 h. The equilibrium concentration of Si is ~0 at.%, which is reached at 1024 h. The time exponents for $\Delta C_i^{\mathrm{int.}}(t)$ (Fig. 12a–c) are -0.16 ± 0.12 for Ni, -0.30 ± 0.07 for Al and -0.20 ± 0.09 for Mn, where the exponents are derived for aging times of 1–1024 h.

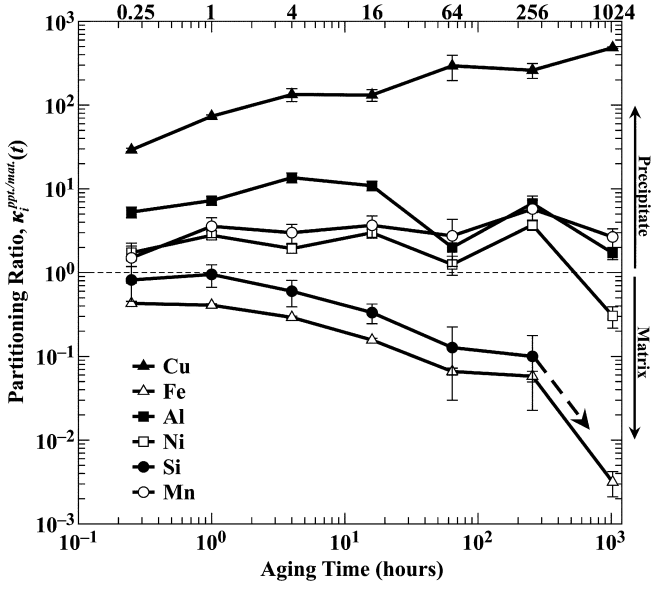

Fig. 9. Partitioning ratios, $\kappa_i^{\mathrm{ppt./mat.}}(t)$, of the concentrated multicomponent Fe–Cu steel as a function of aging time, when aged at 500 °C, from 0.25 to 1024 h. The horizontal dashed line indicates the division between the precipitate and matrix phases. The dashed arrow for the Si ratio represents the zero Si concentration within the precipitate at 1024 h.

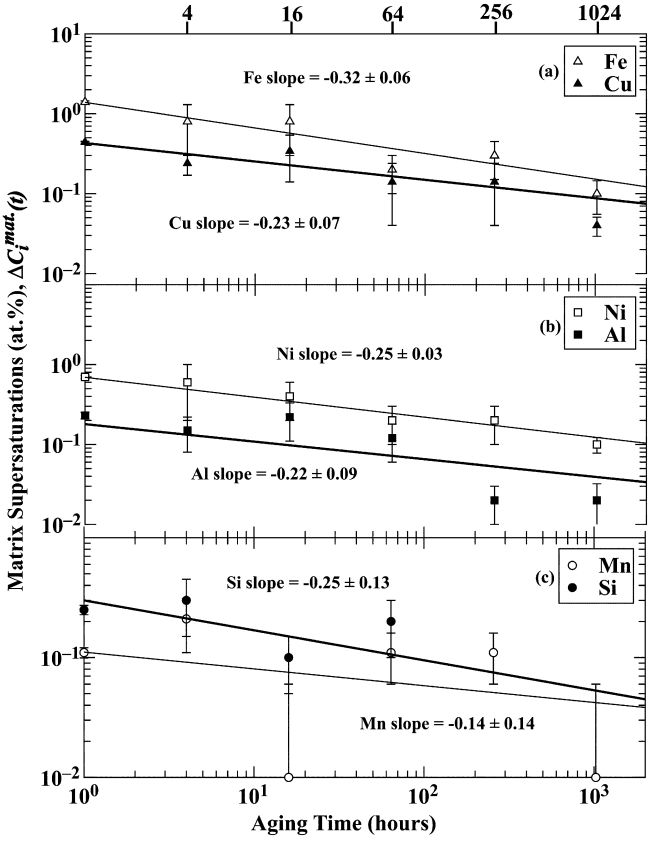

Fig. 10. Double logarithmic plots of matrix supersaturations, $\Delta C_i^{\mathrm{mat.}}(t)$, as a function of aging time, when aged at 500 °C, for (a) Cu and Fe; (b) Ni and Al; and (c) Mn and Si. The slopes of the plots yield the coarsening time exponents for each element.

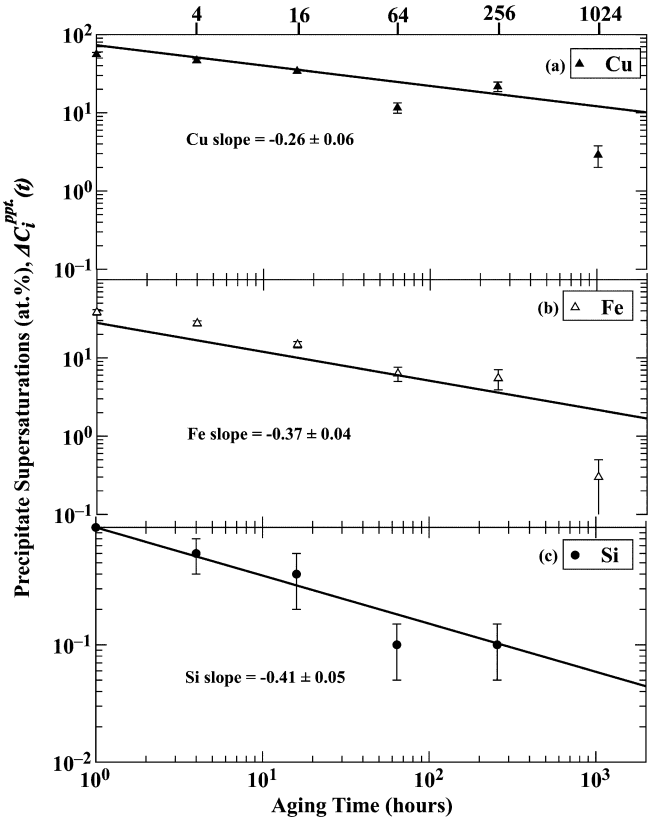

Fig. 11. Double logarithmic plots of the supersaturations in the Cu-rich precipitates cores, $\Delta C_i^{ppt.}(t)$, as a function of aging time, when aged at 500 °C, for (a) Cu, (b) Fe and (c) Si. The slopes of the plots yield the coarsening time exponents for each element.

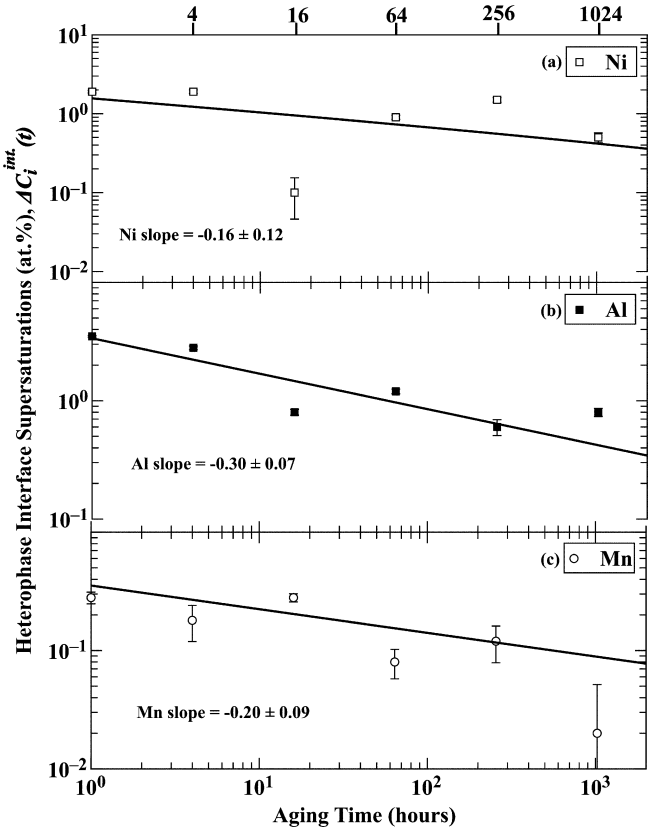

Fig. 12. Double logarithmic plots of the supersaturations in the heterophase interfaces, $\Delta C_i^{int.}(t)$, as a function of aging time, when aged at 500 °C, for (a) Ni, (b) Al and (c) Mn. The slopes of the plots yield the coarsening time exponents for each element.

4. Discussion

4.1. Morphology

The morphologies observed by APT in this investigation are consistent with earlier TEM studies, which show that the bcc Cu → 9R Cu → 3R Cu → fcc ε-Cu phase changes are accompanied by a change from a spheroidal morphology to an ellipsoidal or rod-like morphology [13–16]. Our observation of a rod-like morphology, by APT, in our over-aged Fe–Cu alloy system is, to the best of our knowledge, the first report of such a structure. Transmission electron microscopy observations of the 1024 h aged condition confirm the rod-like morphology of the precipitates (Fig. 13). The precipitates orient along the $[1\,1\,0]_{Cu}\|[1\,1\,1]_{\alpha-Fe}(1\,1\,1)_{Cu}\|(1\,1\,0)_{\alpha-Fe}$ direction, which is the Kurdjumov–Sachs relationship, and is consistent with earlier observations for binary Fe–Cu alloys [13,14,16,20,41,42].

The equilibrium morphology of a precipitate is determined by the balance between elastic and interfacial ener-

Table 5
Extrapolated to infinite time equilibrium compositions of the Cu-rich precipitates, α-Fe matrix and heterophase interfaces compared to measured overall composition at 1024 h and also calculated from Thermo-Calc

		Cu	Al	Ni	Si	Mn	Fe
Extrapolated from APT data to infinite time	Precipitate	100 ± 0.8	0.3 ± 0.2	0.3 ± 0.2	0.1 ± 0.1	0.9 ± 0.2	0
	Interface	10.2 ± 0.2	6.1 ± 0.04	7.1 ± 0.04	1.2 ± 0.04	1.0 ± 0.02	74.3 ± 0.3
	Matrix	0.2 ± 0.008	0.7 ± 0.001	2.2 ± 0.02	1.3 ± 0.02	0.3 ± 0.008	95.2 ± 0.001
Measured from specimens aged 1024 h	Precipitate	97.1 ± 0.8	1.2 ± 0.4	0.7 ± 0.4	0	0.8 ± 0.4	0.3 ± 0.2
	Interface	10.3 ± 0.08	5.2 ± 0.06	6.5 ± 0.07	1.2 ± 0.03	1.0 ± 0.03	75.7 ± 0.1
	Matrix	0.2 ± 0.01	0.7 ± 0.01	2.3 ± 0.02	1.3 ± 0.02	0.3 ± 0.01	95.1 ± 0.04
Calculated from *Thermo-Calc* and SGTE solution database	Precipitate (bcc)	94.2	4.7	0.3	0	0.6	0.3
	Precipitate (fcc)	43.3	2.8	28.2	0	8.5	17.2
	Interface	–	–	–	–	–	–
	Matrix	0.1	1.4	2.2	1.0	0.3	94.9

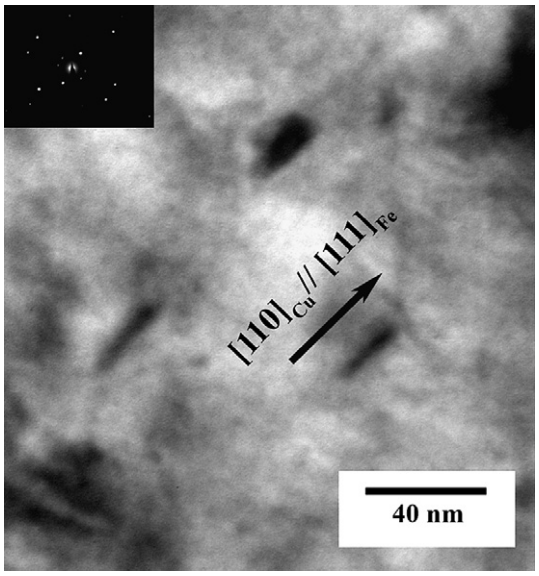

Fig. 13. Bright-field TEM micrograph of the steel when aged at 500 °C for 1024 h. The precipitates are aligned along the Kurdjumov–Sachs orientation: $[1\,1\,0]_{Cu}\|[1\,1\,1]_{\alpha\text{–}Fe}(1\,1\,1)_{Cu}\|(1\,1\,0)_{\alpha\text{–}Fe}$.

gies [43]. Thompson et al. [66] have introduced the L parameter, which represents the equilibrium energy state of a precipitate, and is given by:

$$L = \frac{\delta^2 C_{44} l}{\sigma^{\text{ppt./mat.}}}, \tag{8}$$

where δ is the lattice misfit, C_{44} is an elastic shear modulus, l is a characteristic dimension of the precipitate, and $\sigma^{\text{ppt./mat.}}$ is the precipitate/matrix interfacial free energy. For the purpose of calculating the L parameter we utilize initially values for δ, C_{44} and $\sigma^{\text{ppt./mat.}}$ for a binary Fe–Cu alloy. The quantity $\delta^{\text{fcc-Cu/bcc-Fe}}$ is equal to 0.231 where the lattice parameter, a_0, is equal to 0.3611 nm for Cu (fcc) and 0.28665 nm for α-Fe (bcc) [67]. The remaining quantities are $C_{44}^{\text{fcc-Cu}} = 75$ Gpa [67], which is also approximately the mid-point for the range of reported experimental and simulated values [31,67,68], $l = 13$ nm, and $\sigma^{\text{ppt./mat.}} \approx 600\ \text{mJ m}^{-2}$ [8], where we assume $\sigma^{\text{ppt./mat.}}$ is isotropic. Eq. (8) yields $L = 87$, which suggests an equilibrium morphology controlled solely by the elastic energy. Other reported values for $\sigma^{\text{ppt./mat.}}$ yield similar results. Ludwig et al. [33] report a value of $\sigma^{\text{ppt./mat.}} = 245\ \text{mJ m}^{-2}$ for the sides of a cylindrical precipitate, which gives $L = 212$. Speich and Oriani [14] estimate a value of $\sigma^{\text{ppt./mat.}} = 466\ \text{mJ m}^{-2}$ for the ends of a rod-shaped precipitate, which gives $L = 112$. Monzen et al. [41] report a value of $\sigma^{\text{ppt./mat.}} = 1100\ \text{mJ m}^{-2}$ for the ends of a rod-shaped precipitate, which gives $L = 47$. Lee et al. [69] have shown, however, that the equilibrium morphology of precipitates that are elastically softer than the matrix, such as Cu (fcc) precipitates within an α-Fe (bcc) matrix ($C_{44}^{\text{bcc-Fe}} = 116$ GPa [67] or $C_{44}^{\text{bcc-Fe}} = 101$ GPa [31]), is a platelet, irrespective of elastic anisotropy and orientation relationship. The experimentally observed precipitates possess the twofold symmetry of platelets but also have rounded edges and ellipsoidal bodies, which suggests that both elastic and interfacial energy affect the equilibrium morphology. The differences between our observations and the results of Eq. (8) are partially attributed to an uncertain interfacial energy, which is greater than the reported values, and is also affected by the formation of a Ni–Al–Mn shell, which is discussed below. Aging beyond 1024 h or at higher temperatures may result in a platelet morphology. Other researchers, however, did not observe platelet morphologies in binary Fe–Cu alloys when aging at 500–700 °C for 1000 h [13], or at 730–830 °C for 300 h [14], and at 550 °C for 1000 h [16].

An additional consideration is that the L parameter assumes the same elastic constants for the precipitate and matrix phases, which is not the case for a Cu (fcc) precipitate in an α-Fe (bcc) matrix. Since $C_{44}^{\text{bcc-Fe}}$ is greater than $C_{44}^{\text{fcc-Cu}}$ [67], the difference in elastic constants cannot alone account for the disparity between our observations and the results of Eq. (8). The precipitates, however, are more complicated than a pure binary phase interface. The formation of a Ni–Al–Mn shell also affects the elastic constants and lattice misfit of the Cu-rich precipitates. For the purpose of calculating L we utilize the values of δ, C_{44} and $\sigma^{\text{ppt./mat.}}$ for a binary equiatomic NiAl (B2 structure). For NiAl (B2 structure), $a_0 = 0.2887$ nm [70], yielding $\delta^{\text{B2-NiAl/bcc-Fe}} = 0.0071$. The quantity $C_{44}^{\text{B2-NiAl}} = 114.7$ Gpa [71], which is also approximately the mid-point for the range of reported experimental values [72,73]. Since the interfacial energy of NiAl in α-Fe is unknown we utilize initially the surface energy of NiAl, $\sigma^{\text{ppt./mat.}} \cong 1850\ \text{mJ m}^{-2}$ [70,74], where we assume $\sigma^{\text{ppt./mat.}}$ is isotropic. Since approximately 50% of the Ni and Al bonds at a surface are free, this estimate represents an upper bound for $\sigma^{\text{ppt./mat.}}$. Eq. (8) yields $L = 0.056$, which suggests an equilibrium morphology controlled solely by interfacial energy. A smaller value for $\sigma^{\text{ppt./mat.}}$ would result in a larger L value, but assuming linearity, a 50% reduction in $\sigma^{\text{ppt./mat.}}$ would still yield an equilibrium morphology controlled by interfacial energy.

Clearly, both elastic and interfacial energy contribute to the equilibrium morphology of the precipitates. The ends of the rod-like precipitates are dominated by elastic energy, whereas the sides are controlled by interfacial energy, which is where the Ni, Al and Mn segregation is predominantly found. Other researchers have attributed the rod-like morphology of Cu precipitates in Fe–Cu-based alloys to minimization of elastic strain energy [13] or anisotropy of interfacial energy [14]. This morphology has been attributed to shear associated with partial dislocations producing an invariant plane-strain transformation to the 3R structure from the 9R structure, followed by relaxation to the fcc structure by diffusional growth to minimize interfacial energy [16].

4.2. Coarsening kinetics

Our experimental results indicate nucleation is occurring prior to 0.25 h, nucleation and growth from 0.25 to 1 h,

followed by a transition, and subsequently, after 64 h, an increasing proportion of growth and coarsening. A time-law exponent of 1/2, for diffusion-controlled growth [43,75], however, is not observed, contrary to earlier investigations by TEM [13] and APFIM [6] in model binary Fe–Cu alloys. Assuming coarsening starts at 64 h gives a temporal dependency of $t^{0.34\pm0.09}$ for $\langle R(t)\rangle$, which is in approximate agreement with the UO model value of 1/3 and indicates a diffusion-limited coarsening mechanism. Assuming coarsening starts at 64 h gives a temporal dependency for $N_V(t)$ of $t^{-0.63\pm0.07}$, which is not in agreement with the UO model prediction of −1 and indicates a slower coarsening rate and an admixture of growth and coarsening.

Our results differ from those reported by Speich and Oriani [14] and Monzen et al. [41,42], who report good agreement for the $t^{1/3}$ power-law for $\langle R(t)\rangle$ to aging times of ~300 h. The alloys in their studies are binary Fe–Cu and ternary Fe–Cu–Ni carbon–free alloys, respectively, which can account for the differences with our results. Additionally, the aging temperatures in Ref. [14] were between 730 and 830 °C, and those in Refs. [41,42] were between 600 and 750 °C, which is significantly greater than the 500 °C we employed. At the reported temperatures quasi-stationary state coarsening would be achieved more rapidly than at 500 °C. Our results also differ from the lattice kinetic Monte Carlo simulations of Soisson et al. [27] who obtained a $t^{1/3}$ dependency for $\langle R(t)\rangle$ in a binary Fe–1.34 at.% Cu alloy aged at 300 and 500 °C. Their simulations, however, did not include elastic strain effects, which can have a significant effect on growth and coarsening at longer aging times in a Fe–Cu system.

The time exponents for $\langle R(t)\rangle$ from 1 to 64 h are closer to the 1/6 to 1/4 values predicted for the cluster–diffusion–coagulation coarsening mechanism [43]. The recent observations of Sudbrack et al. [76] and Mao et al. [77] on a model Ni–Al–Cr superalloy indicate that precipitates following such a mechanism would form interconnected necks with clearly delineated lattice planes. We do not, however, observe interconnected necks with lattice planes employing LEAP™ tomography, indicating that the cluster–diffusion–coagulation mechanism is inoperative.

The experimentally determined time exponents for $\Delta C_i^{\text{mat.}}(t)$, with the exception of Fe, do not satisfy the UO model prediction of −1/3. The deviation from the model value of the exponent for Si is possibly due to the rapid approach of the Si matrix concentration to its equilibrium value; Si is a comparatively fast diffusing element in α-Fe (Table 6). The $\Delta C_i^{\text{mat.}}(t)$ time exponents for Cu, Ni, Al and Mn are affected by the bcc Cu → 9R Cu → 3R Cu → fcc ε-Cu [13–16] phase changes of the precipitates and the formation of the Ni–Al–Mn shells. The time exponents for $\Delta C_i^{\text{ppt.}}(t)$ and $\Delta C_i^{\text{int.}}(t)$ are also affected, but more significantly, by the phase changes and formation of the Ni–Al–Mn shell adjacent to the Cu-rich precipitate cores. Within the heterophase interfaces (Fig. 12a–c) only the time exponent for Al is close to, but not exactly identical with, the model prediction, which can possibly be ascribed to the relatively large diffusivity of Al in α-Fe (Table 6). The temporal dependency for Mn is less than that of Al but greater than that of Ni, which corresponds to the diffusivity of Mn, which is slower than that of Al but faster than that of Ni (Table 6). The phase changes affect the solid solubility of Ni, Al and Mn within the Cu-rich precipitates. For example, when the precipitates are <2 nm in radius, which corresponds to the bcc structure, the Mn concentration initially increases from 0.6 ± 0.6 at.% at 0.25 h to 1.5 ± 0.6 at.% at 4 h. The Mn concentration subsequently decreases to 1.1 ± 0.6 at.% at 64 h of aging and then increases to 2.3 ± 1.1 at.% at 256 h, before decreasing to 0.8 ± 0.4 at.% at 1024 h. At an aging time of 1024 h the observed admixture of spheroidal and rod-like precipitates indicates a 9R (spheroidal) and 3R or fcc (ellipsoidal) precipitates. Our observations support the recent phase-field simulations of Koyama et al. [29]. Koyama et al. demonstrated that the Mn concentration increases within the Cu-rich bcc precipitates, but upon transformation to the fcc phase the Mn concentration decreases. The authors did not report the effect of the 9R and 3R phases on Mn concentration.

Table 6
Tracer diffusivities of Cu, Ni, Mn, Si and Al in α-Fe at 500 °C

	D_i (m^2 s^{-1})	Ref.
Cu	1.9×10^{-21}	[78]
Ni	3.4×10^{-21}	[79]
Mn	2.4×10^{-20}	[80]
Si	5.5×10^{-20}	[81]
Al	6.6×10^{-20}	[82]

Our results differ from those of Monzen et al. [41,42], who report agreement with the $t^{-1/3}$ power-law for the kinetics of depletion of supersaturation within the α-Fe matrix. The alloys in their studies are binary Fe–Cu and ternary Fe–Cu–Ni carbon-free alloys and were aged between 600 and 750 °C; these alloys should reach quasi-stationary state coarsening more rapidly than our more complex alloy.

4.3. Composition of the Cu-rich precipitates

4.3.1. Precipitates less than 2 nm in radius

We measure a Fe concentration between 39.9 ± 4.2 and 27.6 ± 2.1 at.% when the Cu-rich precipitates are smaller than 2 nm in radius (Fig. 6a), which corresponds to the bcc structure [5,16,25]. This is consistent with observations in a similar steel, with 1.17 at.% Cu, denoted NUCu-140-1 (140 designates the yield strength in ksi and 1 designates the experimental heat number), where the Fe concentration of the precipitates was measured to be ~25 at.% near-peak hardness [1]. Earlier atom-probe studies of Fe–Cu-based alloys, thermally aged at 500 °C, have also detected significant Fe within Cu-rich precipitates smaller than 2 nm in radius in both binary [8,9,30] and multicomponent [9,10,37] alloys. In contrast to atom-probe measurements, SANS measurements infer, based on several strong assumptions, an Fe concentration

of <10 at.% [21,22]; Fine et al. [83] recently discuss the potential sources of the differences between atom-probe and SANS measurements in binary Fe–Cu alloys. Furthermore, recent first-principles calculations by Liu et al. [31] predict that in a binary Fe–Cu alloy, bcc precipitates with Cu concentrations greater than ~50% are mechanically unstable at 0 K. Although, strictly speaking, the argument of Ref. [31,83] only applies to binary alloys, we also measure a Cu concentration ranging between 44.6 ± 3.1 and 53.5 ± 2.3 at.% when the precipitates are <2 nm in radius. This is consistent with earlier observations for binary [8] and multicomponent [10,37] Fe–Cu-based alloys.

When the precipitates are <2 nm in radius they also contain quantities of Ni, Al, Mn and Si, which is consistent with earlier atom-probe measurements of model ternary Fe–Cu–Ni [9,10] and multicomponent [37] Fe–Cu-based alloys. The recent phase-field simulations of model quaternary Fe–Cu–Ni–Mn alloys also illustrate Cu-rich precipitates containing Ni and Mn at early (non-dimensionless time) stages of phase decomposition [28,29]. Furthermore, the EXAFS results of Pizzini et al. [25] demonstrate that the precipitates retain a bcc structure longer in a model ternary alloy containing Ni, when compared to the binary Fe–Cu alloy. Therefore, the presence of Fe and other alloying elements may be mechanically stabilizing the bcc precipitates.

In the over-aged condition the precipitate cores are enriched in Cu (97.1 ± 0.8 at.%), achieving an almost elemental concentration at 1024 h. This is consistent with earlier atom-probe and SANS investigations of both binary [8,21,84] and ternary [9,10] Fe–Cu-based alloys.

4.3.2. Formation of Ni–Al–Mn shells

Nickel, Al and Mn are found enriched at the precipitate/α-Fe matrix heterophase interfaces as early as 0.25 h of aging (Fig. 7 and Table 4). The observed interfacial segregation becomes more pronounced with increasing aging time, thereby forming a distinct shell containing Ni, Al and Mn adjacent to the Cu-rich precipitate cores at 1024 h. Similar segregation has been observed experimentally and in simulations in over-aged Fe–Cu–Ni [9,10,28,29,35], Fe–Cu–Mn [11,28,29,35], Fe–Cu–Ni–Al [19] and Fe–Cu–Ni–Mn [23,28,29] alloys. Isheim et al. [36–38] have reported comparable segregation effects in similar concentrated multicomponent Fe–Cu steels. At 1024 h the shell has a Ni:Al:Mn stoichiometric ratio of 0.51:0.41:0.08 (Table 7), which suggests a NiAl-type B2 phase with Mn substituting for Al on the latter's sublattice. The conclusion that it has a B2 structure cannot, however, be made by stoichiometry alone. We have recently performed synchrotron radiation studies at the Advanced Photon Source (APS), Argonne, IL, that demonstrate that this shell does indeed have the B2 structure [85]. Furthermore, our recent first-principles calculations confirm that Mn substitutes at Al sublattice sites rather than at Ni sublattice sites [85].

The experimental results illustrate that the shells form by segregation of Ni at the heterophase interfaces with a smaller quantity of Mn and Al also present. The Ni and Mn concentration peaks are initially associated with each other, whereas the Al concentration peak is found closer to the center of the precipitate in possible association with Cu. Further aging results, in increasing interfacial segregation of all three elements, from the matrix and precipitate cores, to the heterophase interfaces; concomitantly the Al concentration peak moves toward the Ni and Mn peaks. As seen from Table 7 the stoichiometric ratio of the heterophase interfaces also evolves temporally, as Al increasingly partitions to the heterophase interfaces. Our observations are in agreement with those of Isheim et al. [37] and Vaynman et al. [1] for the NuCu-140-1 steel and recent phase-field simulations of model quaternary Fe–Cu–Mn–Ni alloys [28,29]. The shells are not homogenous around the Cu-rich cores; as Figs. 3a–c and 4 demonstrate that the interfacial segregation is nonuniform. The Cu-rich precipitates and α-Fe matrix interfaces may be acting as nucleation sites for a $Ni_{0.5}(Al_{0.5-x}Mn_x)$ phase. The observed compositional heterogeneity at the interfaces may also be due to possible trajectory aberrations. Comparable heterogeneous nucleation on Cu precipitates, with nonuniform interfacial segregation, however, has also been reported in amorphous FINEMET alloys [86] and maraging stainless steels [87]. Our observations, however, do not support the three-phase Cu-rich precipitate core, fcc homogeneous shell, and α-Fe matrix model proposed in Ref. [23]. The presence of a $Ni_{0.5}(Al_{0.5-x}Mn_x)$ phase at the precipitate/α-Fe matrix heterophase interfaces is consistent with Cahn's local phase rule for heterophase interfaces [88], which predicts that a single phase at this heterophase interface is permitted thermodynamically.

Table 7
Temporal evolution of Ni:Al:Mn stoichiometric ratio within the heterophase interfaces as a function of aging time

	Ni	Al	Mn
0.25 h	0.57	0.34	0.09
1 h	0.61	0.30	0.08
4 h	0.57	0.35	0.09
16 h	0.54	0.40	0.06
64 h	0.52	0.40	0.08
256 h	0.52	0.41	0.07
1024 h	0.51	0.41	0.08

4.3.3. Equilibrium compositions

Table 5 compares the equilibrium compositions of the Cu-rich precipitate cores, heterophase interfaces and α-Fe matrix derived by three methodologies: (a) extrapolated to infinite time from APT data as a function of $(\text{aging time})^{-1/3}$; (b) as measured from specimens aged for 1024 h; and (c) as calculated from Thermo-Calc utilizing the Scientific Group Thermodata Europe (SGTE) solutions database [89]. Reasonable agreement exists for the first two methodologies but significant differences exist, especially for the Cu-rich precipitates, with the Thermo-Calc calculations. Thermo-Calc predicts the existence of both bcc and

fcc precipitates, with different compositions, for aging at 500 °C. We do not find APT evidence for precipitates with such disparate compositions at the longest aging time we studied, 1024 h; nor do we find, employing conventional X-ray diffraction (XRD) and synchrotron radiation at the APS, evidence for both bcc and fcc precipitates. Additionally, the coexistence of both structures at long aging times is not consistent with earlier TEM investigations of Fe–Cu-based alloys [13–16].

The equilibrium concentrations of Cu, Fe, Ni and Mn within the matrix are similar for all three methodologies. The Thermo-Calc prediction for Si is 1.0 at.%, whereas both APT determined results yield $\sim 1.3 \pm 0.02$ at.%. The greatest variation is present for the concentration of Al, where the APT results of $\sim 0.7 \pm 0.01$ at.%, are one-half the value determined using Thermo-Calc. The measured Cu concentration in the matrix is 0.2 ± 0.01 at.% at 1024 h, which is equal to 0.2 ± 0.008 at.% obtained by extrapolation of our APT data to infinite time and larger than 0.1 at.% predicted by Thermo-Calc. The three values, however, are similar indicating that at 1024 h the Cu matrix concentration is approaching its equilibrium value. Miller et al. [12] reported that the Cu equilibrium matrix concentration is reached after 100 h of aging at 500 °C in a model ternary Fe–Cu–Ni alloy and reported agreement with Thermo-Calc predictions utilizing the Kaufman database.

At an aging temperature of 500 °C Thermo-Calc does not predict the formation of a NiAl-type (B2 structure) phase. At temperatures less than ~480 °C, however, the formation of NiAl precipitates, consisting of 49.6 at.% Al and 50.4 at.% Ni, is predicted. While the existing Thermo-Calc database does not give results that are in exact agreement with our experimental values, it is important that a NiAl phase is predicted at a temperature near 500 °C, indicating that the existence of a B2-type phase is thermodynamically possible. The Ni, Al and Mn enrichments at the heterophase interfaces and the previously reported existence of NiAl-type precipitates at a grain boundary in NUCu-140-1 [1] indicates, however, that the driving force for homogeneous nucleation within the α-Fe matrix is not sufficient, for the given composition and thermal treatment.

The segregation of Ni, Al and Mn observed at 1024 h reduces the interfacial energy of the heterophase interface. The relative Gibbsian interfacial excess, $\Gamma_i^{\text{relative}}$, is the thermodynamic quantity measuring solute segregation of an element i. The relative excess for $i =$ Ni, Al or Mn relative to Fe and Cu is given by [90,91]:

$$\Gamma_i^{\text{Fe,Cu}} = \Gamma_i - \Gamma_{\text{Fe}} \frac{c_i^{\alpha} c_{\text{Cu}}^{\beta} - c_i^{\beta} c_{\text{Cu}}^{\alpha}}{c_{\text{Fe}}^{\alpha} c_{\text{Cu}}^{\beta} - c_{\text{Fe}}^{\beta} c_{\text{Cu}}^{\alpha}} - \Gamma_{\text{Cu}} \times \frac{c_{\text{Fe}}^{\alpha} c_i^{\beta} - c_{\text{Fe}}^{\beta} c_i^{\alpha}}{c_{\text{Fe}}^{\alpha} c_{\text{Cu}}^{\beta} - c_{\text{Fe}}^{\beta} c_{\text{Cu}}^{\alpha}}, \quad (9)$$

where Γ_i is the Gibbsian interfacial excess of an element i, and c_i^j is the concentration of a species i in a phase j ($j = \alpha$ or β), where α refers to the α-Fe matrix phase and β is the Cu-rich precipitate phase. The values for Γ_i and c_i^j are obtained from the proxigrams of Fig. 3c. Greater details regarding the calculation of $\Gamma_i^{\text{Fe,Cu}}$ are given in Ref. [92]. Eq. (9) yields values of $\Gamma_{\text{Ni}}^{\text{Fe,Cu}} = 46.6 \pm 3.0$ atoms nm^{-2}, $\Gamma_{\text{Al}}^{\text{Fe,Cu}} = 46.2 \pm 3.2$ atoms nm^{-2}, $\Gamma_{\text{Mn}}^{\text{Fe,Cu}} = 7.4 \pm 1.4$ atoms nm^{-2}. Thus, significant positive relative Gibbsian interfacial excesses with respect to Fe and Cu exist for Ni, Al and Mn at this heterophase interface.

The reduction in interfacial energy due to segregation, assuming ideal solution behavior, is calculated utilizing the Gibbs adsorption isotherm:

$$\Gamma_i^{\text{Fe,Cu}} = -\frac{c_i}{k_{\text{B}} T} \left(\frac{\partial \sigma^{\text{ppt./mat.}}}{\partial c_i} \right), \quad (10)$$

where c_i is the atomic fraction of an element i within the matrix, k_{B} is Boltzmann's constant, and T is the absolute temperature. Eq. (10) yields a reduction of -625.6 mJ m^{-2} for Ni -620.3 mJ m^{-2} for Al and -99.4 mJ m^{-2} for Mn. The values for Ni and Al exceed the estimated fcc-Cu precipitate and α-Fe matrix $\sigma^{\text{ppt./mat.}}$ values in Refs. [8,14,33] but are approximately 55% of the value reported in Ref. [41]. This suggests that at the ends of the rod-shaped precipitates $\sigma^{\text{ppt./mat.}}$ is greater than the previously reported values for binary Fe–Cu alloys. A larger value of $\sigma^{\text{ppt./mat.}}$ will also reduce the L parameter to a value more in accordance with our experimental observations.

The concentrated multicomponent Fe–Cu steel in this investigation does not strictly obey the UO model asymptotic temporal power laws. The significant differences between the experimentally determined results and the UO model predictions are due to violations of the assumptions of the model. The experimental evidence shows that the morphology of the precipitates become rod-like at longer aging times and are affected by elastic strain energy, the compositions of the Cu-rich precipitates evolve temporally, a $Ni_{0.5}(Al_{0.5-x}Mn_x)$ phase forms at the heterophase interfacial region, the precipitates change phase, and the system has not achieved a quasi-stationary state at 1024 h.

5. Conclusions

The nucleation (to a limited extent), growth and coarsening behavior of Cu-rich precipitates in a concentrated multicomponent Fe–Cu-based steel containing 1.82 at.% Cu (Table 1) was studied experimentally. The steel, denoted NUCu-170 (170 designates the yield strength in ksi), is aged at 500 °C for times between 0.25 and 1024 h. The investigation resulted in the following findings:

1. When the Cu-rich precipitates are less than 2 nm in radius the Cu concentration ranges between 44.6 ± 3.1 and 53.5 ± 2.3 at.% and the Fe content ranges between 39.9 ± 4.2 and 27.6 ± 2.1 at.%.
2. At peak yield strength (4 h aging) the Cu-rich precipitates contain 53.5 ± 2.3 at.% Cu and significant concentrations of Fe, Ni, Al, Mn and Si. The precipitates at 1024 h contain 97.1 ± 0.8 at.% Cu.

3. Copper partitions to the precipitate cores, whereas Ni, Al and Mn partition to the heterophase interfaces, and Fe and Si partition to the α-Fe matrix during aging to 1024 h. The temporal evolution of Ni, Al and Mn concentrations within the precipitate cores and heterophase interfaces are non-monotonic.
4. The Ni:Al:Mn stoichiometric ratio at the heterophase α-Fe matrix/Cu-rich precipitate interfaces is 0.51:0.41:0.08 at 1024 h, which corresponds chemically to the B2 structure with Mn substituting for Al on the latter's sublattice. The segregation of Ni, Al, and Mn at this heterophase interface reduces the interfacial energy by −625.6, −620.3 and −99.4 mJ m^{-2}, respectively.
5. The spherical volume equivalent mean radius, $\langle R(t) \rangle$, increases from 1.2 ± 0.1 nm at 0.25 h to 6.5 ± 0.7 at 1024 h. The temporal dependencies are $t^{0.16}$ between 0.25 to 1 h, $t^{0.16\pm0.01}$ between 1 and 64 h, and $t^{0.34\pm0.09}$ from 64 to 1024 h, in agreement with the UO coarsening model predicted value of 1/3 between only 64 and 1024 h.
6. The number density, $N_V(t)$, increases from $(5.2 \pm 0.8) \times 10^{23}\ m^{-3}$ at 0.25 h to $(4.2 \pm 0.5) \times 10^{24}$ at 1 h. Then the quantity $N_V(t)$ decreases to $(7.4 \pm 0.5) \times 10^{22}\ m^{-3}$ at 1024 h. The temporal dependencies are $t^{2.7}$ between 0.25 to 1 h, $t^{-0.45\pm0.03}$ between 1 and 64 h, and $t^{-0.63\pm0.07}$ from 64 to 1024 h. The coarsening power-law exponents do not satisfy the coarsening model predicted value of −1, indicating a slower rate of coarsening and the lack of achievement of a stationary state.
7. The coarsening power-law time exponents for the matrix supersaturations, $\Delta C_i^{\text{mat.}}(t)$, are -0.23 ± 0.07 for Cu, -0.32 ± 0.06 for Fe, -0.25 ± 0.03 for Ni, -0.22 ± 0.09 for Al, -0.14 ± 0.14 for Mn and -0.25 ± 0.13 for Si. With the exception of Fe, the exponents do not satisfy the UO coarsening model prediction of −1/3. The time exponents for the Cu-rich precipitate core supersaturations, $\Delta C_i^{\text{ppt.}}(t)$, are -0.26 ± 0.06 for Cu, -0.37 ± 0.04 for Fe and -0.41 ± 0.05 for Si, which do not agree with the predicted temporal dependency. The time exponents for the heterophase interface supersaturations, $\Delta C_i^{\text{int.}}(t)$, are -0.16 ± 0.12 for Ni, -0.30 ± 0.07 for Al and -0.20 ± 0.09 for Mn, which do not agree with the value predicted by the coarsening model. These disagreements are most likely due to the lack of achievement of a stationary state.
8. The equilibrium concentrations of the precipitate phase, as determined by APT, do not match those predicted by Thermo-Calc. Reasonable agreement exists for the α-Fe matrix phase.
9. The rod-like precipitates observed by APT and TEM at 1024 h have the Kurdjumov–Sachs orientation relationship. The morphology is affected by both elastic strain energy and interfacial energy and the presence of a $Ni_{0.5}(Al_{0.5-x}Mn_x)$ phase with a B2 structure, adjacent to the Cu-rich precipitates, found at the precipitate/α-Fe matrix heterophase interfaces.
10. From the above conclusions it is clear that it is difficult to describe the temporal coarsening behavior of a concentrated multicomponent alloy using classical coarsening models. An alternative approach is to utilize PrecipiCalc [93], which is a more general approach to the problem of phase decomposition and includes nucleation, growth and coarsening. There are not yet, however, adequate thermodynamic and mobility databases that would allow its use for the Fe–Cu-based steel we are reporting on in this article.

Acknowledgements

This research is supported by the Office of Naval Research (N00014-03-1-0252), Dr. Julie Christodoulou grant officer. Atom-probe tomographic analyses were performed at the Northwestern University Center for Atom-probe Tomography (NUCAPT), and the LEAP™ tomograph was purchased with funding from the NSF-MRI (DMR-0420532, Dr. Charles Bouldin, monitor) and ONR-DURIP (N00014-0400798, Dr. Julie Christodoulou, monitor) programs. Additionally, the LEAP™ tomograph was enhanced in late April 2006 with a picosecond laser with funding from ONR-DURIP (N0014-06-1-0539, Dr. Julie Christodoulou, monitor). This work made use of Central Facilities supported by the MRSEC Program of the National Science Foundation (DMR-0520513) at the Materials Research Center of Northwestern University. The TEM work was performed in the EPIC facility of NUANCE Center at Northwestern University. NUANCE Center is supported by NSF-NSEC, NSF-MRSEC, Keck Foundation, the State of Illinois, and Northwestern University. We extend our gratitude to Professor Emeritus Morris E. Fine, Research Professor Semyon Vaynman, and Research Assistant Professor Dieter Isheim for discussions, and to D.I. for managing NUCAPT.

References

[1] Vaynman S, Isheim D, Kolli RP, Bhat SP, Seidman DN, Fine ME. Metall Mater Trans A 2008;39A:363.
[2] Dhua SK, Mukerjee D, Sarma DS. Metall Mater Trans A 2001;32A:2259.
[3] Czyrycka EJ, Link RE, Wong RJ, Aylor DA, Montemarano TW, Gudas JP. Nav Eng J 1990;102:63.
[4] Montemarano TW, Sack BP, Gudas JP, Vassilaros MG, Vanderveldt HH. J Ship Prod 1986;2:145.
[5] Lahiri SK, Chandra D, Schwartz LH, Fine ME. Trans Metall Soc AIME 1969;245:1865.
[6] Goodman SR, Brenner SS, Low Jr JR. Metall Trans 1973;4:2363.
[7] Youle A, Ralph B. Met Sci J 1972;6:149.
[8] Goodman SR, Brenner SS, Low Jr JR. Metall Trans 1973;4:2371.
[9] Worrall GM, Buswell JT, English CA, Hetherington MG, Smith GDW. J Nucl Mater 1987;148:107.

[10] Pareige PJ, Russell KF, Miller MK. Appl Surf Sci 1996;94/95:362.
[11] Maruyama N, Sugiyama M, Hara T, Tamehiro H. Mater Trans JIM 1999;40:268.
[12] Miller MK, Russell KF, Pareige PJ, Starink MJ, Thomson RC. Mater Sci Eng A 1998;A250:49.
[13] Hornbogen E, Glenn RC. Trans Metall Soc AIME 1960;218:1064.
[14] Speich GR, Oriani RA. Trans Metall Soc AIME 1965;233:623.
[15] Othen PJ, Jenkins ML, Smith GDW, Phythian WJ. Philos Mag Lett 1991;64:383.
[16] Othen PJ, Jenkins ML, Smith GDW. Philos Mag A 1994;70:1.
[17] Monzen R, Jenkins ML, Sutton AP. Philos Mag A 2000;80:711.
[18] Deschamps A, Militzer M, Poole WJ. ISIJ Int 2001;41:196.
[19] Watanabe T. Tetsu-to-Hagané 1975;61:2456.
[20] Charleux M, Livet F, Bley F, Louchet F, Bréchet Y. Philos Mag A 1996;73:883.
[21] Kampmann R, Wagner R. Phase transformations in Fe–Cu-alloys—SANS-experiments and theory. In: Janot C, Petry W, Richter D, Springer T, editors. Atomic transport and defects in metals by neutron scattering, vol. 10. Berlin: Springer-Verlag; 1986. p. 73.
[22] Osamura K, Okuda H, Takashima M, Asano K, Furusaka M. Mater Trans JIM 1993;34:305.
[23] Osamura K, Okuda H, Asano K, Furusaka M, Kishida K, Kurosawa F, et al. ISIJ Int 1994;34:346.
[24] Osamura K, Okuda H, Ochiai M, Takashima M, Asano K, Furusaka M, et al. ISIJ Int 1994;34:359.
[25] Pizzini S, Roberts KJ, Phythian WJ, English CA, Greaves GN. Philos Mag Lett 1990;61:223.
[26] Maury F, Lorenzelli N, Mathon MH, de Novion CH, Lagarde P. J Phys: Condens Mater 1994;6:569.
[27] Soisson F, Barbu A, Martin G. Acta Mater 1996;44:3789.
[28] Koyama T, Onodera H. Mater Trans 2005;46:1187.
[29] Koyama T, Hashimoto K, Onodera H. Mater Trans 2006;47:2765.
[30] Zhang C, Enomoto M, Yamashita T, Sano N. Metall Mater Trans A 2004;35A:1263.
[31] Liu JZ, van de Walle A, Asta MD. Phys Rev B 2005;72:144109.
[32] Blackstock JJ, Ackland GJ. Philos Mag A 2001;81:2127.
[33] Ludwig M, Farkas D, Pedraza D, Schmauder S. Modell Simul Mater Sci Eng 1998;6:19.
[34] Nagano T, Enomoto M. Scripta Mater 2006;55:223.
[35] Zhang C, Enomoto M. Acta Mater 2006;54:4183.
[36] Isheim D, Gagliano MS, Fine ME, Seidman DN. Acta Mater 2006;54:841.
[37] Isheim D, Kolli RP, Fine ME, Seidman DN. Scripta Mater 2006;55:35.
[38] Isheim D, Seidman DN. Surf Interface Anal 2004;36:569.
[39] Lifshitz IM, Slyzov VV. J Phys Chem Solids 1961;19:35.
[40] Wagner CZ. Electrochem 1961;65:581.
[41] Monzen R, Takada K, Matsuda K. Z Metallkd 2003;94:1241.
[42] Monzen R, Takada K, Watanabe C. ISIJ Int 2004;44:442.
[43] Wagner R, Kampmann R, Voorhees PW. Homogeneous second-phase precipitation. In: Kosortz G, editor. Phase transformations in materials. Weinheim: Wiley-VCH; 2001. p. 309.
[44] Ratke L, Voorhees PW. Growth and coarsening: ripening in material processing. Berlin: Springer-Verlag; 2002.
[45] Umantsev A, Olson GB. Scripta Metall Mater 1993;29:1135.
[46] Kuehmann CJ, Voorhees PW. Metall Mater Trans A 1996;27A:937.
[47] Vaynman S, Fine ME, Lee S, Espinosa HD. Scripta Mater 2006;55:351.
[48] Vaynman S, Isheim D, Fine ME, Seidman DN, Bhat SP. Recent advances in high-strength, low-carbon, precipitation-strengthened ferritic steels. Materials science and technology 2004, vol. 1. New Orleans, LA: AIST and TMS; 2004.
[49] Miller MK. Atom probe tomography. New York: Kluwer Academic/Plenum; 2000.
[50] Tsong TT. Atom-probe field ion microscopy. Cambridge: Cambridge University Press; 1990.
[51] Kelly TF, Gribb TT, Olson JD, Martens RL, Shepard JD, Wiener SA, et al. Microsc Microanal 2004;10:373.
[52] Seidman DN. Annu Rev Mater Res. 2007;37:127.
[53] Hellman OC, Blatz du Rivage J, Seidman DN. Ultramicroscopy 2003;95:199.
[54] Hellman OC, Vandenbroucke JA, Rüsing J, Isheim D, Seidman DN. Microsc Microanal 2000;6:437.
[55] Kolli RP, Seidman DN. Microsc Microanal 2007;13:272.
[56] Miller MK, Kenik EA. Microsc Microanal 2004;10:336.
[57] Sudbrack CK, Noebe RD, Seidman DN. Phys Rev B 2006;73:212101.
[58] Sudbrack CK. Decomposition behavior in model Ni–Al–Cr–X superalloys: temporal evolution and compositional pathways on a nanoscale. Evanston, IL: Northwestern University; 2004.
[59] Gagliano MS, Fine ME. CALPHAD: Comput Coupling Phase Diagrams Thermochem 2001;25:207.
[60] Gagliano MS, Fine ME. Metall Mater Trans A 2004;35A:2323.
[61] Russell KF, Brown LM. Acta Metall 1972;20:969.
[62] Barbu A, Mathon MH, Maury F, Belliard JF, Beuneu B, de Novion CH. J Nucl Mater 1998;257:206.
[63] Sudbrack CK, Isheim D, Noebe RD, Jacobson NS, Seidman DN. Microsc Microanal 2004;10:355.
[64] Meyer SL. Data analysis for scientists and engineers. New York: John Wiley; 1975.
[65] Yoon KE, Noebe RD, Seidman DN. Acta Mater 2007;55:1159.
[66] Thompson ME, Su CS, Voorhees PW. Acta Metall Mater 1994;42:2107.
[67] Harry T, Bacon DJ. Acta Mater 2002;50:195.
[68] Overton Jr WC, Gaffney J. Phys Rev 1955;98:969.
[69] Lee JK, Barnett DM, Aaronson HI. Metall Trans A 1977;8A:963.
[70] Miracle DB. Acta Metall Mater 1993;41:649.
[71] Jiang C, Sordelet DJ, Gleeson B. Acta Mater 2006;54:2361.
[72] Davenport T, Zhou L, Trivisonno J. Phys Rev B 1999;59:3421.
[73] Rusović N, Warlimont H. Phys Status Solidi A 1977;44:609.
[74] Mutasa B, Farkas D. Surf Sci 1998;415:312.
[75] Zener C. J Appl Phys 1949;20:950.
[76] Sudbrack CK, Yoon KE, Noebe RD, Seidman DN. Acta Mater 2006;54:3199.
[77] Mao Z, Sudbrack CK, Yoon KE, Martin G, Seidman DN. Nat Mater 2007;6:210.
[78] Salje G, Feller-Kniepmeier MJ. J Appl Phys 1977;48:1833.
[79] Hirano K, Cohen M, Averbach BL. Acta Metall 1961;9:440.
[80] Irmer V, Feller-Kniepmeier MJ. J Phys Chem Solids 1972;33:2141.
[81] Bergner D, Khaddar Y, Lörx S. Defect Diffus Forum 1990;66–69:1407.
[82] Akimova IA, Mironov VM, Pokoyev AV. Phys Met Metallgr 1983;56:175 [English translation].
[83] Fine ME, Liu JZ, Asta MD. Mater Sci Eng A 2007;463:271.
[84] Auger P, Pareige PJ, Akamatsu M, Van Duysen J-C. J Nucl Mater 1994;211:194.
[85] Kolli RP, Mao Z, Keane DT, Seidman DN. Appl Phys Lett 2007;91:241903.
[86] Hono K, Ping DH, Ohnuma M, Onodera H. Acta Mater 1999;47:997.
[87] Hättestrand M, Nilson J-O, Stiller K, Liu P, Andersson M. Acta Mater 2004;52:1023.
[88] Cahn JW. J Phys (Paris) 1982:43 [Conference C6:199].
[89] Thermo-Calc. Stockholm: Thermo-Calc Software.
[90] Dregia SA, Wynblatt P. Acta Metall Mater 1991;39:771.
[91] Defay R, Prigogine I, Bellemans A, Everett DH. Surface tension and adsorption. New York: Wiley; 1966.
[92] Kolli RP, Yoon KE, Seidman DN; in preparation.
[93] Jou H-J, Voorhees PW, Olson GB. Computer simulations for the prediction of microstructure/property variation in aeroturbine disks. In: Green KA, Pollock TM, Harada H, Howson TE, Reed RC, Schirra JJ, Walston S, editors. Tenth international symposium on superalloys; 2004. p. 877.